

Early Diagnosis of Triple-Negative Breast Cancer Based on Dual microRNA Detection Using a Well-Defined DNA Crown-Carbon Dots Structure as an Electrochemiluminescence Sensing Platform

Zhuoxin Ye, Mo Ma, Yuxuan Chen, Jukun Yang, Chen Zhao, Quanping Diao, Pinyi Ma,* and Daqian Song*



Cite This: *Anal. Chem.* 2024, 96, 17984–17992



Read Online

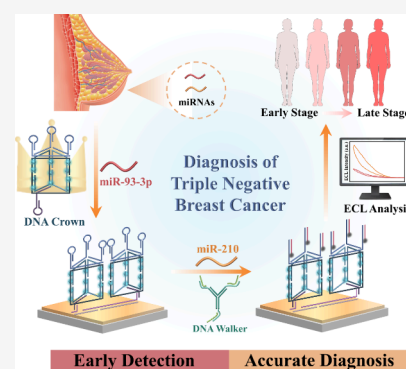
ACCESS |

Metrics & More

Article Recommendations

Supporting Information

ABSTRACT: Triple-negative breast cancer (TNBC) is the most aggressive subtype of breast cancer (BC). Thus, early detection and accurate diagnosis of this cancer are crucial for improving the survival rate of patients. Specific microRNAs (miRNAs) have been implicated in the occurrence, proliferation, and metastasis of TNBC. Addressing this need, our study developed a biosensor platform for early and accurate TNBC diagnosis by integrating electrochemiluminescence (ECL) technology with a DNA sensing strategy. Specifically, synthesized positively charged carbon dots (CDs) were used to neutralize the electrostatic repulsion between DNA strands and facilitate the assembly of DNA triangular prisms (DNA TP-CDs). Hairpins were then incorporated into the DNA TP-CDs to form the final DNA crown structure. The early TNBC biomarker, microRNA-93–3p (miR-93–3p), allowed for the binding between the DNA Crown and the DNA track on the electrode and initiated the ECL signal. Subsequently, microRNA-210 (miR-210) unlocked the DNA tripedal walker, and its movement on the DNA Crown eventually quenched the ECL signal, enabling accurate TNBC diagnosis and tumor stage assessment. Our proposed biosensor had satisfactory sensing efficiency due to the ordered DNA track and rapid-moving DNA walker. The data revealed a good linear relationship between the ECL signals and the logarithm of miRNA concentrations, with miR-93–3p having a detection limit of 31.04 aM and miR-210 having a detection limit of 7.69 aM. The biosensor also showed satisfactory performance in serum samples and cells. Taken together, this study hopes to provide ideas and applications for clinical diagnosis as well as the personalized treatment of TNBC.



INTRODUCTION

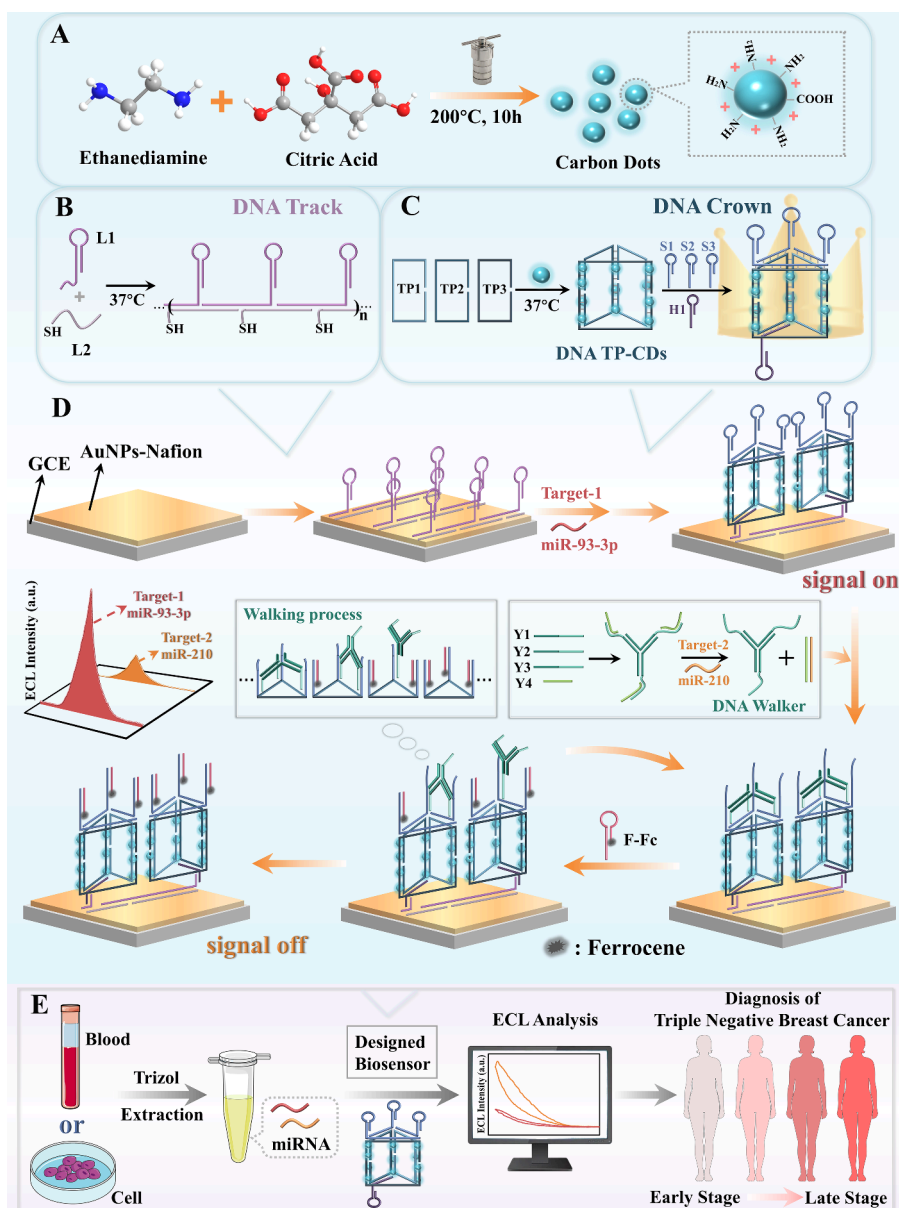
Breast cancer (BC) is one of the most prevalent malignant tumors and the leading cause of cancer-related deaths among women globally. Triple-negative breast cancer (TNBC) lacks expression of estrogen receptor (ER), progesterone receptor (PR), and human epidermal growth factor receptor 2 (HER2), accounting for 10–25% of all BC cases.^{1–4} Compared with other BC subtypes, TNBC is highly invasive, often associated with distant metastases, poor prognosis, and shorter overall and disease-free survival of patients, which is the greatest difficulty in clinical intervention.^{5–9} The lack of effective early detection methods often leads to late-stage diagnosis, which significantly lowers patient survival rates. Thus, the development of advanced assays to identify early TNBC biomarkers is critical for improving early diagnosis.^{9,10} Beyond early detection, precise diagnosis and accurate tumor staging are also essential for personalized clinical treatment of BC, offering the potential to significantly enhance patient outcomes.

MicroRNAs (miRNAs) are a family of small noncoding RNAs consisting of 21–25 nucleotides. It has been reported that dysregulated miRNAs may regulate a variety of signaling pathways and promote the occurrence, progression, and metastasis of BC.^{11–13} Therefore, miRNAs can provide critical

information for BC subtype-specific diagnosis, early detection, staging, and prognosis of TNBC.¹⁴ Li et al. showed that miR-93–3p is overexpressed in TNBC patients and promotes stem cellularization, drug resistance, and metastasis of TNBC cells. Importantly, this overexpression is observed even in the early stages of TNBC, suggesting that miR-93–3p could serve as a reliable biomarker for early detection.⁹ Furthermore, miR-210 is overexpressed under hypoxic conditions, especially in highly invasive TNBC subtypes, which affects the process of tumor development and promotes BC proliferation, and its expression level is positively correlated with tumor stage.^{15–17} Based on the above points, miRNA levels can not only provide essential information for early prediction and accurate diagnosis of TNBC but also monitor subsequent tumor development and stages.

Received: June 11, 2024
Revised: October 17, 2024
Accepted: October 21, 2024
Published: October 31, 2024



Scheme 1. Schematic Diagram of an “Off–On–Off” ECL Sensing Platform for Dual-miRNA Detection^a

^a(A) Synthesis of positively charged CDs. (B) Preparation of highly ordered DNA track. (C) Assembly of DNA TP-CDs and DNA Crown. (D) Construction of the ECL biosensor platform for the quantitative detection of miR-93-3p and miR-210. (E) Application of the designed biosensor in the diagnosis of triple-negative breast cancer.

Detecting multiple miRNAs remains a challenging task due to their low abundance, high homology, and short sequences.^{18,19} Achieving accurate detection of multiple miRNAs simultaneously is crucial for providing comprehensive diagnostic information and has substantial clinical value. A variety of analytical tools have been developed for the sensitive detection of miRNAs.^{20–24} Among them, electrochemiluminescence (ECL) stands out in modern analytical chemistry for miRNA detection due to its remarkable sensitivity, strong controllability, and low background noise.^{25–29} For instance, Jie and team developed a dual-wavelength ECL biosensor with intramolecular self-enhancement properties based on nanocomposites for the simultaneous detection of miR-141 and miR-155.³⁰ Similarly, Han et al. reported Ru- and luminol-doped dual-wavelength ECL Janus emitters with dual-miRNA detection capability.³¹ Current multitarget ECL sensors share

common features: they typically involve loading ECL emitters onto electrodes and connecting signal probes, where the presence of the target miRNA alters the ECL signal. These platforms often rely on potential or wavelength resolution, which necessitates the cumbersome labeling of multiple signal probes. Therefore, developing efficient and straightforward multitarget ECL sensors remains a significant challenge.

Recently, Qian and colleagues proposed that positively charged materials could substitute for Mg^{2+} to neutralize negatively charged DNA to mediate the self-assembly of DNA nanostructures, and the materials can be bound to DNA nanostructures.^{32,33} We envision inducing DNA assembly into a well-defined nanostructure using a positively charged ECL emitter, introducing this structure onto the electrode surface in the presence of the target, and simultaneously forming a sensing platform for the next detection step. Based on this

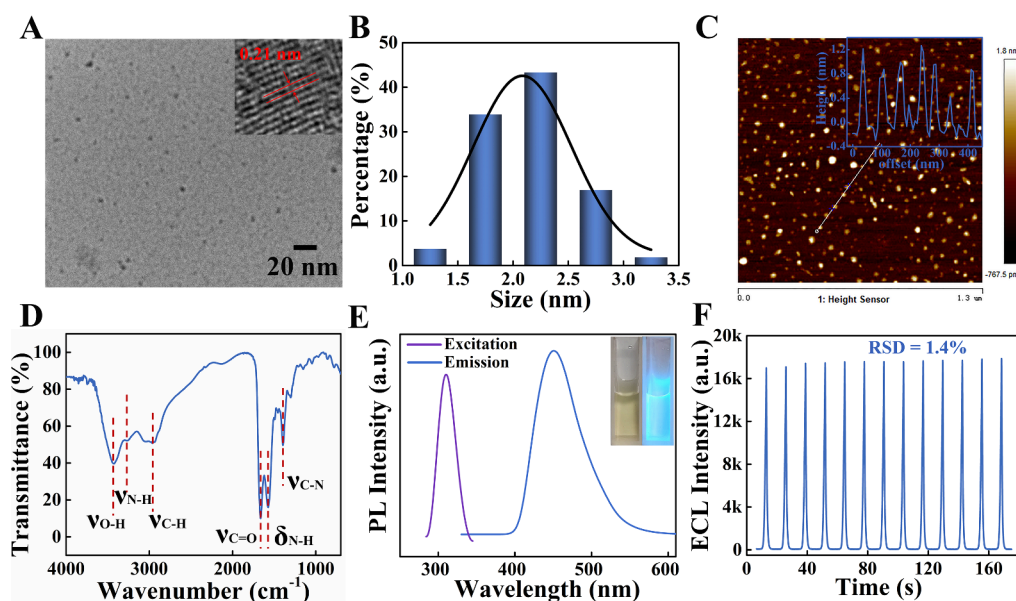


Figure 1. Characterization of CDs. (A) TEM image of CDs at 20 nm scale. The inset shows the lattice spacing of CDs. (B) Particle size distribution of CDs. (C) AFM image of CDs (Inset: height profile along the white line). (D) FT-IR spectra of CDs. (E) FL excitation and emission spectra of CDs (Inset: images of CDs under visible light (left) and UV light (right)). (F) ECL stability of CDs after 13 cycles of continuous scanning.

concept, constructing an efficient, fast, and simple ECL sensing platform with dual detection functions is valuable for research in this field.

Inspired by the above discussion, this study proposed an ECL response-based strategy for dual-miRNA detection by utilizing positively charged carbon dots (CDs) to mediate the assembly of the DNA triangular prism (DNA TP-CDs) framework to construct the sensing platform. Meanwhile, an ordered linear stepped DNA track and a DNA tripodal walker moving along a predetermined trajectory were introduced to enhance sensing efficiency. Specifically, nitrogen-rich CDs exhibited a positive charge due to the protonation of nitrogen, thus neutralizing the electrostatic repulsion between DNA strands and initiating the assembly of DNA into the designed DNA TP structure. Subsequently, hairpins were hybridized at both the bottom and top of the DNA TP to act as capture probes for two-step sensing, resulting in a crown-like framework (referred to as the “DNA Crown”). Target-1, miR-93-3p, drove the integration of the DNA Crown into the tracks on the electrode surface (an “off-on” switch), at which point the hairpin at the top of the DNA Crown forms a new track. Next, target-2, miR-210, released the locked tripodal walker, whose movement along the tracks at the top of the DNA Crown eventually quenched the ECL signals (an “on-off” switch). By combining the DNA sensing technique with ECL, the biosensor can provide a promising approach for the early detection and staging of TNBC (for detailed design principles of the ECL biosensor, please refer to the [Supporting Information 2.1](#)).

EXPERIMENTAL SECTIONS

Preparation of DNA TP-CDs and DNA Crown. Equal molar of DNA TP1, TP2, and TP3³⁴ were mixed in positively charged CD solutions (final concentrations of the CD solutions were 0.35, 0.7, 1.5, 3, 5, and 8 mg/mL). The mixture was assembled into the DNA TP-CD structure by annealing or an isothermal reaction, and the assembly effects

were compared. For annealing, the mixture was heated at 95 °C for 10 min and then slowly cooled to 25 °C at a rate of 1 °C/1 min. For the isothermal assembly of the DNA TP-CD structure, the DNA strands were mixed and incubated at 4, 22, 37, and 42 °C for 2 h to obtain the optimal reaction temperature. In addition, the isothermal self-assembly time (from 0.5 h to overnight), as well as the solution pH (from 5 to 9), was varied to obtain the optimal reaction conditions.

Next, four DNA strands (H1, S1, S2, and S3) were dissolved in Tris buffer and annealed to form hairpin structures. Then, these four hairpins (with the same final concentration as that of DNA TP) were mixed with DNA TP-CDs and incubated at 37 °C for 2 h. Eventually, to form the DNA Crown structure, the bottom of the DNA TP-CDs was connected to H1, and the top was connected to S1, S2, and S3 ([Scheme 1C](#)).

Preparation of DNA Track and Locked DNA Tripodal Walker. First, L1 was annealed at 95 °C for 10 min and then slowly cooled to room temperature to form the hairpin structure. The sulfhydryl-modified L2 strand was pretreated with 1 M tris(2-carboxyethyl)-phosphine hydrochloride (TCEP) at 37 °C for 30 min to reduce disulfide bonds.³⁵ Finally, the mixture of L1 and L2 (both 2 μM) in Tris buffer was reacted at 37 °C for 2 h to form the DNA track ([Scheme 1B](#)).³⁶

Then, Y1, Y2, Y3 (1 μM), and Y4 (3 μM) were mixed in Tris buffer and incubated at 37 °C for 3 h to form the tripodal walker, and Y4 locked the walker ([Scheme 1D](#)) for subsequent sensing.

Assembly of ECL Biosensor Platform. The glassy carbon electrode (GCE, Φ = 4 mm) was polished with alumina powder and ultrasonically cleaned with deionized water and ethanol. Subsequently, 10 μL of a AuNP-Nafion mixture (by mixing AuNP suspension and 1% Nafion, volume ratio 4:1)^{37,38} was dropped on the surface of the GCE and dried to obtain AuNPs/GCE. After that, 8 μL of the prepared 2 μM DNA track (L1-L2-SH) solution was bound to the electrode through Au-S bonds at 37 °C for 3 h. After incubation, the

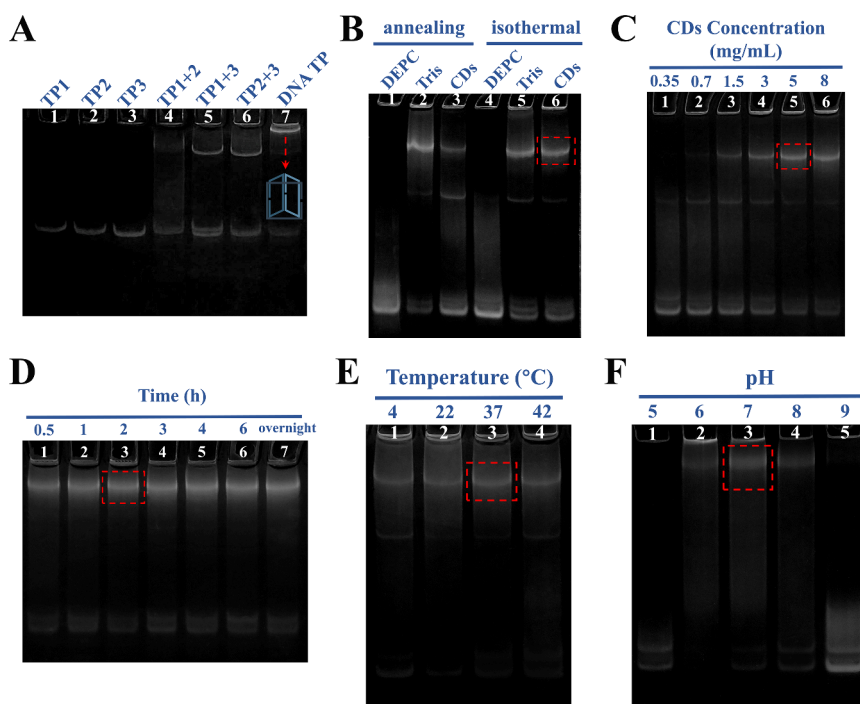


Figure 2. PAGE analysis of DNA TP-CD assembly (concentration of DNA strands = 1.5 μM). (A) DNA TP formation in Tris buffer. (B) Assembly of DNA TP in different solutions and comparison between annealing and isothermal (37 $^{\circ}\text{C}$) assembly. Assembly of DNA TP-CDs using CDs at different concentrations (C), at different reaction times (D), at different reaction temperatures (E), and at different pH values (F).

unbound DNA track was washed with deionized water to obtain the ECL biosensor platform (DNA track/AuNPs/GCE) for subsequent detection (Scheme 1D).

ECL Measurement. The quantitative detection of miR-93-3p was performed by measuring the enhanced ECL signal. First, the DNA Crown (2 μM) was mixed with different concentrations of the target miR-93-3p. Then, 8 μL of the mixture was dropped onto the modified electrode (DNA track/AuNPs/GCE) and reacted at 37 $^{\circ}\text{C}$ for 70 min to allow binding between H1 on the DNA Crown and L1 on the DNA track, resulting in the modified electrode (DNA Crown/DNA track/AuNPs/GCE). After the unbound DNA Crown was washed off, the ECL signal was recorded.

Next, the quantitative detection of miR-210 was performed based on the sensing of miR-93-3p in the first part. The DNA Crown was connected to the DNA track of the electrode using miR-93-3p at a fixed concentration (the highest concentration of the linear curve), and the corresponding ECL signals were used as constants in the following miR-210 detection. Different concentrations of miR-210 were added to the prepared locked tripodal walker and incubated at 37 $^{\circ}\text{C}$ for 2 h to allow for the release of the tripodal walker. Subsequently, the F-Fc strand (1.5 μM) was mixed with the released tripodal walker, and 8 μL of the mixture was dropped onto the electrode to initiate the movement of the tripodal walker along the top of the DNA Crown. During this process, F-Fc hybridized to the DNA Crown (F-Fc/DNA Crown/DNA track/AuNPs/GCE). After incubation at 37 $^{\circ}\text{C}$ for 60 min, the unhybridized F-Fc strand was rinsed off, and the ECL signal was recorded (Scheme 1D). The ECL response was measured in a solution of 0.1 M PBS (2 mL) containing 10 mM $\text{S}_2\text{O}_8^{2-}$ by using an MPI-E ECL system. The working potential was set from -2 to 0 V, and the scan rate was 300 mV/s (photomultiplier high voltage of 800 V, amplitude 4).

RESULTS AND DISCUSSION

Morphology, Structure, and Optical Characterizations of CDs. The morphology and size of CDs were characterized by transmission electron microscopy (TEM). The TEM image (Figure 1A) showed that the CDs were uniformly distributed on the copper mesh with a good

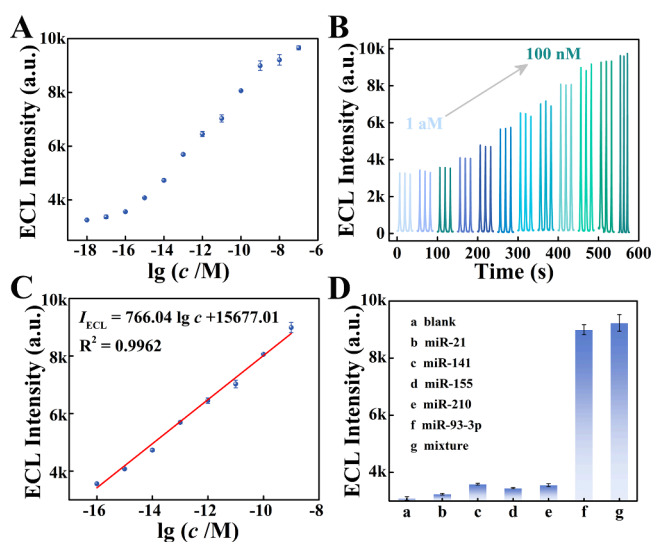


Figure 3. Analytical performance of the ECL biosensor in miR-93-3p detection. (A) Response of the ECL biosensor to miR-93-3p at different concentrations (1 aM, 10 aM, 100 aM, 1 fM, 10 fM, 100 fM, 1 pM, 10 pM, 100 pM, 1 nM, 10 nM, and 100 nM). (B) Stability of the ECL biosensor. (C) Calibration curve showing the relationship between ECL intensity and the logarithmic value of miR-93-3p concentration ($n = 3$, from 100 aM to 1 nM). (D) Specificity of the proposed biosensor.

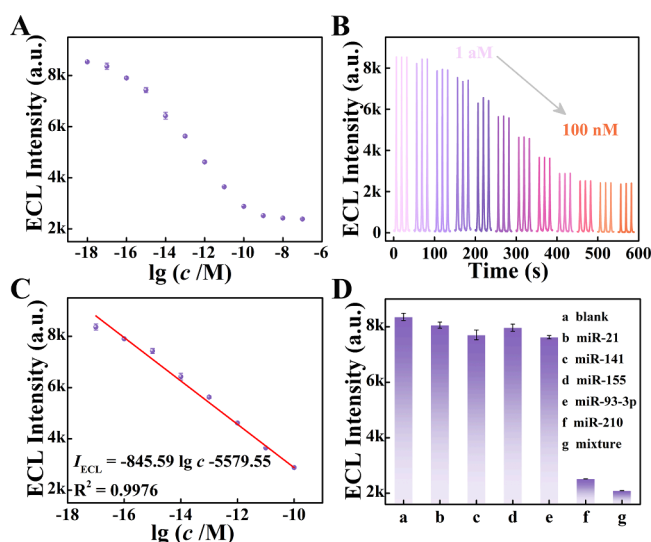


Figure 4. Analytical performance of the prepared ECL biosensor in miR-210 detection. (A) Response of the ECL biosensor to miR-210 at different concentrations (1 aM, 10 aM, 100 aM, 1 fM, 10 fM, 100 fM, 1 pM, 10 pM, 100 pM, 1 nM, 10 nM, and 100 nM). (B) Stability of the ECL biosensor. (C) Calibration curve showing the relationship between ECL intensity and the logarithmic value of miR-210 concentration ($n = 3$, from 10 aM to 100 pM). (D) Specificity of the proposed biosensor.

dispersibility. The average diameter of the CDs was about 2.1 nm (Figure 1B), and the lattice spacing was 0.21 nm (Figure 1A, inset), which matched with the (100) diffraction plane of graphite.³⁹ Meanwhile, the white line in the atomic force microscopy (AFM) images showed that the height of CDs was around 1 nm (Figure 1C), which corresponds to the height of 3–4 layers of graphene.

The structural properties of CDs were studied by Fourier transform infrared (FT-IR) spectroscopy. As shown in Figure 1D, CDs exhibited characteristic peaks at 3422, 3269, 2966, 1662, and 1394 cm^{-1} , which correspond to the stretching vibrations of O–H, N–H, C–H, C=O, and C–N, respectively. Additionally, the peak at 1571 cm^{-1} represented the N–H bending vibration.⁴⁰ The FT-IR results indicated the presence of hydroxyl, amino, and carboxyl groups in CDs. The fluorescence (FL) spectrum showed that the maximum excitation wavelength of CDs was 310 nm, and the optimum emission peak was 460 nm (Figure 1E). Finally, the ECL strength and stability of CDs were measured after they were dropped onto the electrode. As shown in Figure 1F, after 13 consecutive scanning cycles, CDs still exhibited strong (average intensity = 17,535 a.u.) and stable ECL (relative standard deviation = 1.4%), which proves that the CDs have excellent ECL performance, as reported in the literature.^{41–43}

Characterization and Optimization of DNA TP-CDs.

The assembly of DNA TP in the presence of Mg^{2+} (in Tris buffer) was characterized by polyacrylamide gel electrophoresis. As exhibited in Figure 2A, lanes 1–6 represent TP1, TP2, TP3, TP1 + TP2, TP1 + TP3, and TP2 + TP3, respectively, and lane 7 represents TP1 + TP2 + TP3. As can be seen, lane 7 had the lowest mobility, which is indicative of the successful assembly of DNA TP. Subsequently, to explore the ability of positively charged CDs to assemble DNA TP in the absence of Mg^{2+} , we performed comparative experiments on the assembly efficiency of DNA TP in different solutions, including DEPC water, Tris buffer (containing Mg^{2+}), and

aqueous solutions of CDs. TP1, TP2, and TP3 were mixed, annealed at 95 °C, and then slowly cooled to room temperature. The PAGE results (Figure 2B, lane 3) showed that positively charged CDs indeed contributed to the formation of DNA TP, and the DNA single strands TP1, TP2, and TP3 did not spontaneously assemble into DNA TP in the absence of the cation (Figure 2B, lane 1). CD-mediated DNA TP had a clear band and the same mobility on the gel as Mg^{2+} -assembled DNA TP; however, its assembly efficiency was lower compared to Mg^{2+} -assembled DNA TP. To improve the efficiency of CD-assembled DNA TP, we compared the annealing assembly with the isothermal assembly. Interestingly, it can be seen that the isothermal assembly at 37 °C could greatly improve the efficiency of CD-mediated DNA TP assembly (Figure 2B, lane 6).

Afterward, we conducted a series of optimization experiments to improve assembly efficiency. As the concentration of CDs was increased, the DNA TP-CD bands began to appear, and the highest yield was achieved when the CD concentration reached 5 mg/mL (Figure 2C). When the reaction time was extended from 0.5 h to overnight, the reaction had a high assembly efficiency, even at 0.5 h, and the yield remained almost unchanged after 2 h (Figure 2D). Then, the temperature for the assembly of DNA TP-CDs was varied to 4, 22, 37, and 42 °C. Figure 2E shows that the best assembly occurred at 37 °C. Ultimately, Figure 2F demonstrates that the yield of DNA TP-CDs was low or even almost nonexistent when the pH of the reaction system was lower than 6 or higher than 8. The pH range for the isothermal self-assembly of DNA TP-CDs was between 6 and 8, and the highest assembly efficiency was achieved at pH 7, which is in the proximity of physiological pH and an indication of their potential in biological applications.

Under the optimal conditions, the feasibility of sequential hybridization of H1, S1, S2, and S3 hairpins to DNA TP-CDs was verified. As shown in Figure S10B, with the increase of hairpins, the position of the hybridization product bands on the polyacrylamide gel was gradually higher, which confirms the successful formation of the DNA Crown (PAGE analysis of the sensing strategy in Supporting Information 2.8).

Optimization of Reaction Conditions and Comparison of Walking Rate of DNA Walkers. To achieve optimal experimental performance, it is necessary to optimize important experimental parameters. First, the effect of the DNA Crown concentration and reaction time on the electrode was investigated. As shown in Figure S15A, the ECL signal increased significantly as the DNA Crown concentration was increased from 0.5 to 4 μM , and the increasing rate slowed down after 2 μM ; thus, the DNA Crown concentration used in subsequent experiments was 2 μM . Next, as the reaction time of the DNA Crown on the electrode was prolonged, the ECL intensity showed an upward trend and remained stable after 70 min (Figure S15B). Thus, the optimum reaction time for immobilizing the DNA Crown onto the electrode was 70 min. In the detection of miR-210, the F-Fc concentration (quenched ECL signal) was another important factor affecting the experiment. It can be clearly observed in Figure S15C that the ECL signal decreased sharply with the increase of F-Fc concentration and reached a plateau at 1.5 μM , which was thus considered the optimal concentration for F-Fc.

To investigate the performance and optimal walking time of the designed DNA tripedal walker, the kinetic data of the walking were studied by time-dependent ECL analysis and

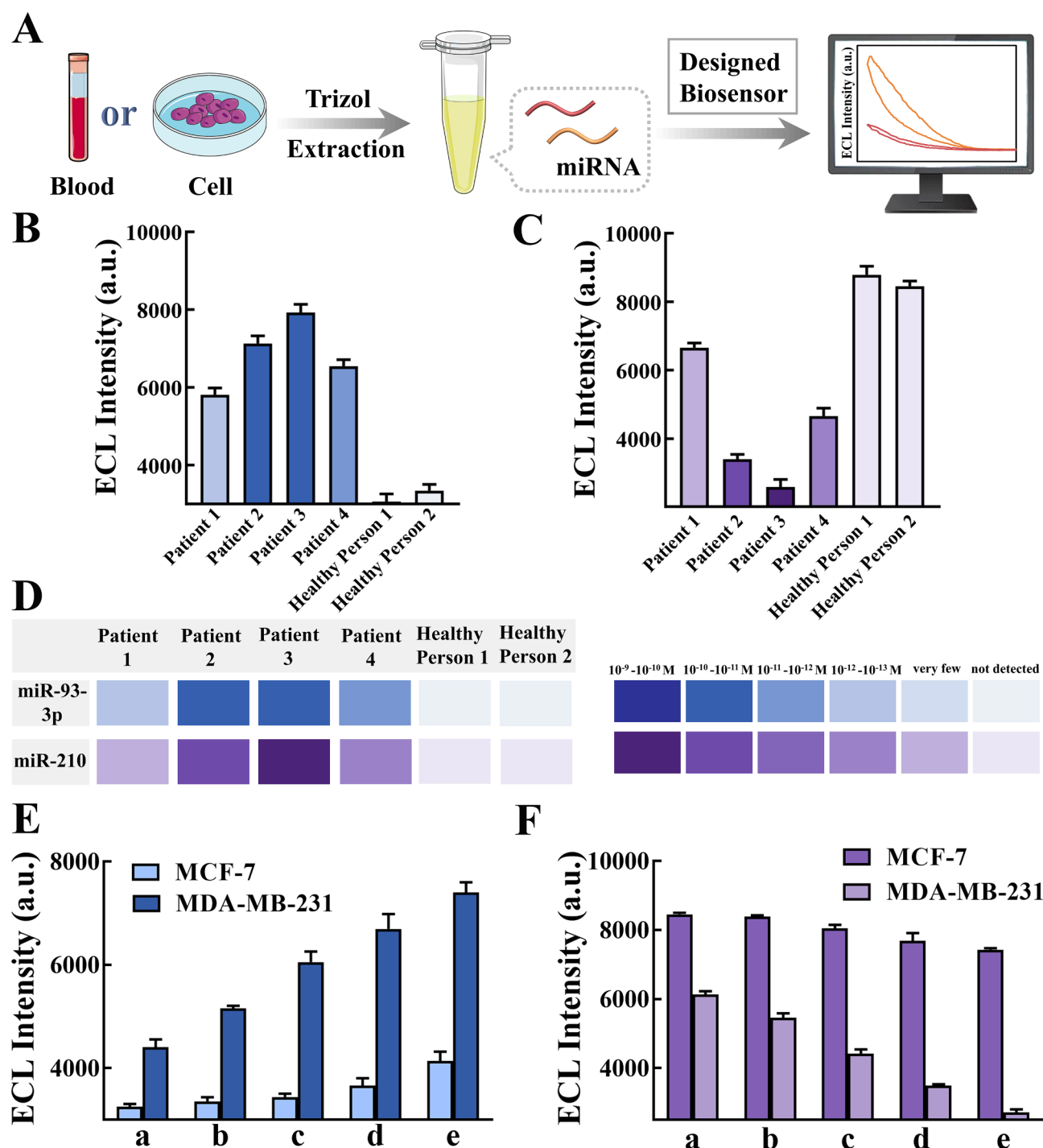


Figure 5. Applications of the biosensor in serum and cells. (A) Schematic diagram of the biosensor being applied to serum and cells. ECL biosensor-based detection of (B) miR-93-3p and (C) miR-210 in the serum of patients and healthy persons. (D) Comparison of two miRNA levels in different patients and healthy persons. ECL biosensor-based detection of (E) miR-93-3p and (F) miR-210 in MCF-7 and MDA-MB-231 cells at different cell numbers: (a) 2×10^1 , (b) 2×10^2 , (c) 2×10^3 , (d) 2×10^4 , and (e) 2×10^5 cells.

compared with those of the conventional DNA monopodal walker and DNA bipodal walker. As shown in Figure S15D–F, after the monopodal, bipodal, and tripodal walkers (mixed with the F-Fc strand) were incubated on the electrode surface, the ECL intensity decreased significantly and reached a plateau, where the reaction was completed at 115, 85, and 60 min, respectively. Thus, it could be concluded that the tripodal walker had the highest walking rate. At the same time, the walking speed (k) of the tripodal walker (the absolute value of

the slope of the ECL intensity-time curve) was also the largest. The above results demonstrate that the designed tripodal walker is highly suitable for the proposed sensing platform, with a high walking efficiency.

Performance of ECL Biosensor in miR-93-3p Detection. Under the optimal conditions, the ECL signals of the biosensor for detecting miR-93-3p at different concentrations (from 1 aM to 100 nM) were measured. As displayed in Figure 3A,B, the ECL intensity increased continuously with the

increase of miR-93-3p concentration, and the intensity corresponding to each concentration was also relatively stable. After analysis, a satisfactory linear correlation between ECL intensity (I_{ECL}) and the logarithm of miR-93-3p concentration ($\lg c$) was observed in the range of 100 aM–1 nM (Figure 3C). The linear regression equation of the fitted curve could be expressed as $I_{\text{ECL}} = 766.04 \lg c + 15677.01$ ($R^2 = 0.9962$), and the limit of detection (LOD) was 31.04 aM ($S/N = 3$).

The specificity of the ECL biosensor was assessed through interference tests, wherein common BC biomarkers (miR-21, miR-141, and miR-155) and the second part of target miR-210 were selected as interfering molecules. In Figure 3D, despite their high concentration (10 nM), the ECL response of the interferents was slightly changed. However, at a lower concentration (1 nM) of miR-93-3p, a significant increase in the intensity of the signal was observed. The ECL signal for a mixture containing interfering substances and miR-93-3p was almost the same as that of miR-93-3p alone. The above results illustrate that the platform has high specificity for miR-93-3p.

Performance of ECL Biosensor in miR-210 Detection.

Next, miR-93-3p at a fixed concentration (1 nM) was added to the system, and the ECL signal obtained was used as the initial signal for the detection of target-2 miR-210 at different concentrations. As the concentration of miR-210 was increased from 1 aM to 100 nM, the ECL intensity gradually decreased (Figure 4A,B). Meanwhile, a linear relationship was observed between ECL intensity and the logarithmic value of miR-210 concentration in the range of 10 aM–100 pM. The linear regression equation for the calibration curve was $I_{\text{ECL}} = -845.59 \lg c - 5579.55$ ($R^2 = 0.9976$), and the LOD was 7.69 aM (Figure 4C).

Similarly, the specificity of the biosensor to miR-210 was also evaluated. Interferents including miR-21, miR-141, miR-155 (each at 1 nM), and target-1 miR-93-3p (100 pM) were selected for the comparative experiment. In Figure 4D, when miR-210 was present (including the mixture), the ECL signal significantly decreased compared to the signals of other interferents. This proves that the ECL biosensor can specifically detect miR-210.

Application of ECL Biosensor in Analysis of Actual Samples. Next, we collected blood from several TNBC patients, extracted the miRNAs using the Trizol lysis method (Supporting Information), and detected them using the biosensor. Combined with Figure 5B–D, miR-93-3p and miR-210 were barely detectable in the serum of healthy persons. Comparing the miRNA levels of these patients, it was found that patients 2 and 3 had higher levels of miR-93-3p, while patient 3 had higher levels of miR-210 than patient 2. Therefore, we can preliminarily determine that the staging of patient 3 is relatively high. Meanwhile, if the patient has a high level of miR-93-3p in the blood, miR-210 will also show a high level. Based on the above results, it can be concluded that the proposed ECL biosensor is feasible for detecting dual miRNAs in actual samples as well as for the diagnosis of TNBC.

Finally, to further verify its practicability, the biosensor was applied to analyze cancer cells. First, total miRNAs were extracted from the cells using the Trizol lysis method and used in the following tests (Figure 5A). MCF-7 cells and MDA-MB-231 (from TNBC) cells at different cell numbers (from 2×10^1 to 2×10^5 cells) were used as test samples for comparison.

Figure 5E demonstrates an increase in the ECL signal caused by miR-93-3p in cells at various cell numbers. It was clear that the ECL signal corresponding to MDA-MB-231 was significantly enhanced as the number of cells increased, even at low cell numbers. In contrast, the ECL signal of MCF-7 cells was only slightly increased, suggesting that the miR-93-3p level was high in MDA-MB-231 cells. As depicted in Figure 5F, miR-210 in both cell types quenched the ECL signal. By contrast, the ECL intensity of MDA-MB-231 decreased more significantly as the cell number increased, indicating that the miR-210 level in MDA-MB-231 cells was much higher than that in MCF-7 cells. These results demonstrate that the proposed biosensor can be applied well to the detection of TNBC biomarkers.

CONCLUSIONS

In conclusion, an “off–on–off” ECL biosensor was successfully constructed based on the assembly of a DNA Crown mediated by positively charged CDs, and a sensing platform for the early and accurate diagnosis of TNBC through miR-93-3p and miR-210 levels was successfully built. Meanwhile, the biosensor combined the DNA track designed in a highly ordered manner and the DNA tripedal walker moving along a predetermined trajectory; thus, its sensing efficiency was greatly improved. Target-1, miR-93-3p, could immobilize the DNA crown, which bound CDs, onto the DNA track of the electrode through the CHA process, thereby turning on the ECL signal and allowing for the early detection of TNBC. Next, the DNA tripedal walker, opened by miR-210, moved along the top of the DNA crown, eventually leading to the quenching of the ECL signal and allowing for the further accurate diagnosis of TNBC and assessment of tumor stages. The results demonstrated that the designed biosensor showed outstanding performance in detecting miR-93-3p and miR-210 and was successfully applied to the analysis of real samples. It is expected that our proposed biosensor can be applied for the early diagnosis and clinical management of TNBC to improve the survival rate of patients.

ASSOCIATED CONTENT

Supporting Information

The Supporting Information is available free of charge at <https://pubs.acs.org/doi/10.1021/acs.analchem.4c02986>.

Additional experimental details, reagents, apparatus, sequence information for the DNA oligonucleotides, strand diagram of the assembled DNA structures, synthesis of Au nanoparticles, steps for extracting total miRNAs from cells by Trizol method, optical and structure characterization of CDs, ECL mechanism of the CDs/ $\text{S}_2\text{O}_8^{2-}$ system, zeta potentials characterization, AFM characterization, PAGE analysis of sensing strategies, characterization of the modified electrode, ECL intensity-potential plot, detection limit, supplementary figures, and supplementary tables and references (PDF)

AUTHOR INFORMATION

Corresponding Authors

Pinyi Ma – College of Chemistry, Jilin Province Research Center for Engineering and Technology of Spectral Analytical Instruments, Jilin University, Changchun 130012, China;

orcid.org/0000-0002-3230-4928; Email: mapinyi@jlu.edu.cn

Daqian Song – College of Chemistry, Jilin Province Research Center for Engineering and Technology of Spectral Analytical Instruments, Jilin University, Changchun 130012, China; Liaoning Key Laboratory of Development and Utilization for Natural Products Active Molecules, School of Chemistry and Life Science, Anshan Normal University, Anshan 114005, China; orcid.org/0000-0002-4866-1292; Email: songdq@jlu.edu.cn

Authors

Zhuoxin Ye – College of Chemistry, Jilin Province Research Center for Engineering and Technology of Spectral Analytical Instruments, Jilin University, Changchun 130012, China

Mo Ma – College of Chemistry, Jilin Province Research Center for Engineering and Technology of Spectral Analytical Instruments and School of Pharmacy, Jilin University, Changchun 130012, China

Yuxuan Chen – College of Chemistry, Jilin Province Research Center for Engineering and Technology of Spectral Analytical Instruments, Jilin University, Changchun 130012, China

Jukun Yang – College of Chemistry, Jilin Province Research Center for Engineering and Technology of Spectral Analytical Instruments, Jilin University, Changchun 130012, China

Chen Zhao – College of Chemistry, Jilin Province Research Center for Engineering and Technology of Spectral Analytical Instruments, Jilin University, Changchun 130012, China

Quanping Diao – Liaoning Key Laboratory of Development and Utilization for Natural Products Active Molecules, School of Chemistry and Life Science, Anshan Normal University, Anshan 114005, China

Complete contact information is available at:

<https://pubs.acs.org/10.1021/acs.analchem.4c02986>

Notes

The authors declare no competing financial interest.

ACKNOWLEDGMENTS

This work was supported by the National Natural Science Foundation of China (22074052 and 22004046) and the Science and Technology Developing Foundation of Jilin Province of China (20230101033JC and 20240404044ZP).

REFERENCES

- (1) Zhang, C.; Tang, S.; Wang, M.; Li, L.; Li, J.; Wang, D.; Mi, X.; Zhang, Y.; Tan, X.; Yue, S. *ACS Nano* **2024**, *18*, 5470–5482.
- (2) Liu, J.; Zhang, L.; Zeng, W.; Zhang, L.; He, N.; Lu, Z. *Chin. Chem. Lett.* **2023**, *34*, No. 108141.
- (3) Zhao, B.; Ma, Z.; Ding, S.; Cao, Y.; Du, J.; Zeng, L.; Hu, Y.; Zhou, J.; Zhang, X.; Bian, X. W.; Tian, G. *Adv. Funct. Mater.* **2023**, *33*, No. 2306328.
- (4) Liu, Q.; Chen, X.; Jiang, Y.; Yan, M.; Yu, B.; Zhang, W.; Cen, Y.; Zhang, J.; Zhang, J.; Lei, Q.; Li, S.; Yang, B. *Adv. Funct. Mater.* **2023**, *34*, No. 2311677.
- (5) Powrózek, T.; Ochieng Otieno, M. *Cancers* **2022**, *14*, 803.
- (6) Vagia, E.; Mahalingam, D.; Cristofanilli, M. *Cancers* **2020**, *12*, 916.
- (7) Eghlimi, R.; Shi, X.; Hrovat, J.; Xi, B.; Gu, H. *J. Proteome Res.* **2020**, *19*, 2367–2378.
- (8) Abramson, V. G.; Lehmann, B. D.; Ballinger, T. J.; Pietenpol, J. A. *Cancer* **2015**, *121*, 8–16.

(9) Li, H.-Y.; Liang, J.-L.; Kuo, Y.-L.; Lee, H.-H.; Calkins, M. J.; Chang, H.-T.; Lin, F.-C.; Chen, Y.-C.; Hsu, T.-I.; Hsiao, M.; Ger, L.-P.; Lu, P.-J. *Breast Cancer Res.* **2017**, *19*, 133.

(10) Yin, L.; Duan, J.-J.; Bian, X.-W.; Yu, S.-C. *Breast Cancer Res.* **2020**, *22*, 61.

(11) Zhong, W.; Liang, Z.; Zhao, H.; Wang, P.; Li, Z.; Shi, J.; Ma, Q. *Biosens. Bioelectron.* **2023**, *240*, No. 115663.

(12) Angius, A.; Cossu-Rocca, P.; Arru, C.; Muroli, M. R.; Rallo, V.; Carru, C.; Uva, P.; Pira, G.; Orrù, S.; De Miglio, M. R. *Cancers* **2020**, *12*, 3298.

(13) Cantini, L.; Bertoli, G.; Cava, C.; Dubois, T.; Zinovyev, A.; Caselle, M.; Castiglioni, L.; Barillot, E.; Martignetti, L. *Nucleic Acids Res.* **2019**, *47*, 2205–2215.

(14) Tang, Q.; Ouyang, H.; He, D.; Yu, C.; Tang, G. *Artif. Cells Nanomed. Biotechnol.* **2019**, *47*, 2800–2809.

(15) Mao, H.; Cao, Y.; Zou, Z.; Xia, J.; Zhao, J. *Chem. Sci.* **2023**, *14*, 2097–2106.

(16) Qattan, A.; Al-Tweigeri, T.; Alkhalaf, W.; Suleman, K.; Tulbah, A.; Amer, S. *Genes* **2021**, *12*, 549.

(17) Ke, H.-L.; Li, W.-M.; Lin, H.-H.; Hsu, W.-C.; Hsu, Y.-L.; Chang, L.-L.; Huang, C.-N.; Li, C.-C.; Chang, H.-P.; Yeh, H.-C.; Li, C.-F.; Wu, W.-J. *Int. J. Med. Sci.* **2017**, *14*, 578–584.

(18) Cai, R.; Wu, K.; Chen, H.; Chen, X.; Zhang, Y.; Wang, X.; Zhou, N. *Anal. Chem.* **2023**, *95*, 18199–18206.

(19) Su, J.; Du, J.; Ge, R.; Sun, C.; Qiao, Y.; Wei, W.; Pang, X.; Zhang, Y.; Lu, H.; Dong, H. *Anal. Chem.* **2022**, *94*, 13108–13116.

(20) Liu, Y.; Wang, C.; Zhang, C.; Chen, R.; Liu, B.; Zhang, K. *ACS Sens.* **2022**, *7*, 2320–2327.

(21) Luo, W.; Wu, C.; Huang, S.; Luo, X.; Yuan, R.; Yang, X. *Anal. Chem.* **2020**, *92*, 15573–15578.

(22) Sun, W.; Zhang, N.; Ren, X.; Wu, D.; Jia, Y.; Wei, Q.; Ju, H. *Biosens. Bioelectron.* **2023**, *242*, No. 115750.

(23) Zhang, H.; Huang, X.; Liu, J.; Liu, B. *Chem. Sci.* **2020**, *11*, 3812–3819.

(24) Zhao, Q.; Pan, B.; Long, W.; Pan, Y.; Zhou, D.; Luan, X.; He, B.; Wang, Y.; Song, Y. *Nano Lett.* **2022**, *22*, 9714–9722.

(25) Meng, X.; Pang, X.; Yang, J.; Zhang, X.; Dong, H. *Small* **2023**, *20*, No. 2307701.

(26) Li, H.; Yang, Q.; Wang, Z.; Li, F. *ACS Sens.* **2023**, *8*, 1529–1535.

(27) Liu, L.; Liu, Y.; Zhang, Y.; Yuan, R.; Wang, H. *Anal. Chem.* **2022**, *94*, 7191–7199.

(28) Sun, Y.; Fang, L.; Han, Y.; Feng, A.; Liu, S.; Zhang, K.; Xu, J.-J. *Anal. Chem.* **2022**, *94*, 7035–7040.

(29) Zhou, Y.-Y.; Li, G.-F.; Ma, R.-X.; Lin, Y.; Wu, J.-W.; Wu, Y.-Y.; Yan, J.; Liu, S.-G.; Tan, X.-C.; Huang, K.-J. *Anal. Chem.* **2023**, *95*, 14052–14060.

(30) Yin, T.; Wu, D.; Du, H.; Jie, G. *Biosens. Bioelectron.* **2022**, *217*, No. 114699.

(31) Han, T.; Ma, C.; Wang, L.; Cao, Y.; Chen, H. Y.; Zhu, J. *J. Adv. Funct. Mater.* **2022**, *32*, No. 2200863.

(32) Liu, Q.; Xia, J.; Yu, Q.; Gu, P.; Yuan, Y.; Liu, K.; Huang, C.; Chen, C.; Guo, X.; Qian, H. *Macromol. Biosci.* **2022**, *22*, No. 2200248.

(33) Wu, D.; Li, B. L.; Zhao, Q.; Liu, Q.; Wang, D.; He, B.; Wei, Z.; Leong, D. T.; Wang, G.; Qian, H. *Small* **2020**, *16*, No. 1906975.

(34) Peng, R.; Zheng, X.; Lyu, Y.; Xu, L.; Zhang, X.; Ke, G.; Liu, Q.; You, C.; Huan, S.; Tan, W. *J. Am. Chem. Soc.* **2018**, *140*, 9793–9796.

(35) Lu, J.; Wang, J.; Hu, X.; Gyimah, E.; Yakubu, S.; Wang, K.; Wu, X.; Zhang, Z. *Anal. Chem.* **2019**, *91*, 7353–7359.

(36) Lv, H.; Chen, A.; Cheng, W.; Kong, L.; Zhao, M.; Ding, S.; Ju, H.; Cheng, W. *Anal. Chem.* **2020**, *92*, 15624–15631.

(37) Lan, L.; Song, X.; Kuang, X.; Sun, X.; Kuang, R. *Anal. Chem.* **2023**, *95*, 14659–14664.

(38) Qi, H.; Li, M.; Dong, M.; Ruan, S.; Gao, Q.; Zhang, C. *Anal. Chem.* **2014**, *86*, 1372–1379.

(39) Guo, Y.-Z.; Yang, Y.-T.; Chen, Y.-F.; Liu, J.-L.; Chai, Y.-Q.; Yuan, R. *Anal. Chem.* **2023**, *95*, 7021–7029.

(40) Chen, B. B.; Liu, M. L.; Zhan, L.; Li, C. M.; Huang, C. *Z. Anal. Chem.* **2018**, *90*, 4003–4009.

- (41) Cao, Y.; Zhou, Y.; Lin, Y.; Zhu, J.-J. *Anal. Chem.* **2021**, *93*, 1818–1825.
- (42) Chen, A.; Liang, W.; Wang, H.; Zhuo, Y.; Chai, Y.; Yuan, R. *Anal. Chem.* **2020**, *92*, 1379–1385.
- (43) Guo, Y.-Z.; Liu, J.-L.; Chen, Y.-F.; Chai, Y.-Q.; Li, Z.-H.; Yuan, R. *Anal. Chem.* **2022**, *94*, 7601–7608.